Surge protection device digital prototyping

Olga Schneider[1], Arnd Ehrhardt[1], Bernd Leibig[1], Sebastian Schmausser[1],
Andrey Aksenov[2] and Elena Shaporenko[2]

[1] DEHN SE + Co KG, Hans-Dehn-Straße 1, 92318 Neumarkt, Germany, olga.schneider@dehn.de

[2] Capvidia NV, Technologielaan 3, 3001 Leuven, Belgium

Abstract

The market requirements for surge protection devices (SPD) call for improvements of their technical parameters, characterized by; higher impulse currents, higher short-circuit currents and at the same time reduced size. This leads to a significantly increased level of complexity for the tools used in design, simulation, and production. Another very crucial business aspect is time to market, forcing shorter development cycles. Implementing the SPD digital prototyping workflow into design cycle reduces both the development time and development costs. This paper presents virtual spark gap model development steps and simulation results of the real physical processes occurring in a spark gap-based SPD device. The virtual spark gap simulation is based on the full compressible Navier-Stokes equations, the energy conservation law, the radiation heat transfer and Maxwell equations. Presented simulation results include arc behaviour, gas flow dynamics and electromagnetic forces. The results are validated using a high-speed camera for arc visualization and compared with experimental data. This virtual simulation technology shows the ability for the further increase of product reliability, performance and size optimization.

1 Introduction and background

To ensure high quality products, it is necessary to consider market requirements, which are constantly becoming more complex for SPD products. In line with market trends, performance characteristics, such as impulse and short-circuit currents, are becoming higher and the size of the product needs to get smaller. These requirements force the design team to increase their efforts to add more physical design loops in the SPD standard development process, see Fig. 1a. In each loop of the standard workflow, a physical test must be executed at the laboratory. This is a very time-consuming process and puts a lot of strain on expensive and highly loaded laboratory resources. The digital prototyping is an ideal concept to reduce these efforts.
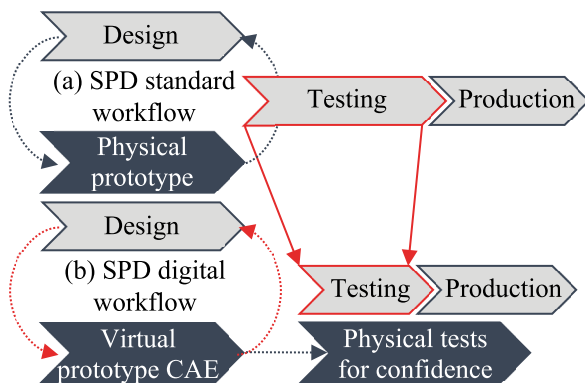

Fig. 1 Product design process and comparison of the SPD standard workflow (a) with the SPD digital workflow (b).

The SPD digital workflow (Fig. 1b) is based on virtual testing, which includes design and downstream computer-aided engineering (CAE) simulation. Computer simulation enables product optimization without the need for physical tests in the laboratory. Physical tests are only necessary to ensure confidence in the final design. Comparison of the digital workflow with the standard workflow (see Fig.1) shows that the digital process can reduce the time required for product development and provide significant cost savings.

The content of this paper is focused on the SPD digital prototyping based on spark gaps. Modern lightning and overvoltage arresters are mainly integrated into low-voltage installations, such as DIN-rail devices. SPD devices are installed directly at the entry point of the power and data lines onto the building or installations. These devices provide potential equalization and protection of electrical and electronic equipment against high-energy, conducted and field-based interference. After the lightning current arrester has operated due to an overvoltage, impulse currents flow to earth. In case of spark-gap-based lightning current arresters, an arc discharge occurs, and the separation gap is ionized. The impulse current is followed by the mains current controlled by the mains voltage. Spark gaps with arc splitters or deionization chambers have a high follow current extinguishing capability and follow current limitation in case of both alternating and direct currents. The important requirements for modern lightning protection systems [1, 2] are divided into the following main topics. SPD devices must be able to safely extinguish the prospective short-circuit current in the system several times. Effective encapsulation of arresters is required to prevent the release of hazardous ionized

gases, especially under loads with high lightning impulse currents. Particularly relevant is a space-saving rule that uses the horn principle with asymmetrical shapes. Therefore, along with the physical properties of the plasma, the electrodynamic spark gap processes and hot gas control play a crucial role in product development to determine whether the arc will be able to extinguish in time to keep the device operational. The optimization of the geometric and gasdynamic parameters can only be achieved in combination with the plasma physical processes. Due to the complex multiphysical processes, digital prototyping is highly useful for the further development of modern SPD devices.

The basic principle of the lightning current arrester with its most important components, including the essential spark gap processes, is shown in Fig. 2.
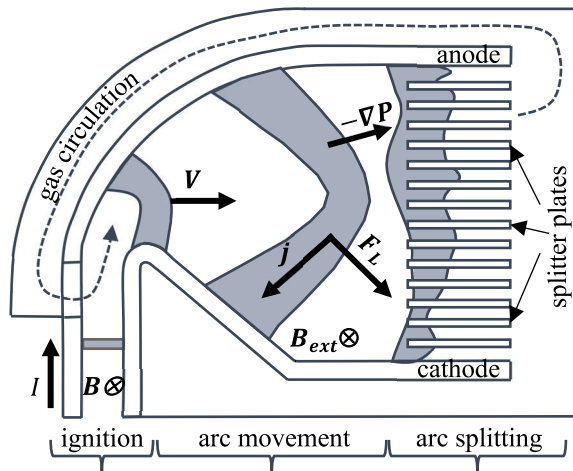

Fig. 2 Schematic diagram of the lightning current arrester and spark gap processes.

The lightning protection device consists of two electrodes and an extinguishing chamber. The distance between these electrodes increases in a horn-shaped and asymmetric way from the ignition area over the arc movement area to the arc splitting chamber. The chamber has many ferromagnetic splitter plates with a V-shaped recess. In the practical implementation [1, 2] the splitter plates are fixed in a plastic support with exhaust openings, so that the gases released from the chamber are directed through special channels in the housing. The outer casing of the device is fully encapsulated to prevent interference with the environment. The overvoltage triggers the lightning current arrester. The electrical current flows from the anode to the cathode as the electric field intensity reaches values higher than the breakdown electric intensity of the gas [3]. The electrical arc occurs in the ignition area between the diverging electrodes. The electrical arc in the lightning arrester is supported by two sources. Impulse current is the ignition source, which can be triggered by 10/350 μs or 8/20 μs waveforms and then accompanied by the mains following current. During ignition a high pressure is generated by intense gas heating. Due to the pressure gradient and Lorentz force, the arc moves in the direction of the splitter plates, see Fig. 2. Some

lightning protection devices include ferromagnetic concentration plates, which create an additional magnetic field to increase the Lorentz force. During the splitting process, the arc starts to stretch around the splitter plates and the voltage rises for forming the arc roots on the plates. When the current flowing through the plates reaches the total current, the arc splits into small parts.

In order to describe these spark gap processes, the three-dimensional virtual spark gap model for SPD digital prototyping is developed. The model is based on the FlowVision computational fluid dynamics (CFD) code [10]. The mathematical model reflects the real physical processes of spark gap formation and is based on the compressible Navier-Stokes equations, the energy conservation law, Maxwell equations for electric and magnetic fields and the radiation heat transfer equations.

There are many publications about arc numerical models [4, 5, 6, 7, 8], where arc simulation frameworks consist of two or more separate solvers working on different numerical domains. These frameworks require additional software for solvers synchronization and their data exchange. In this work, the arc model is based on the magnetohydrodynamic approach (MHD), where the gas flow solver and the electromagnetic equations are solved conjointly on one simulation domain, which uses the finite volume method (FVM).

For the simulation of the arc motion and splitting processes, the arc root model at the gas-solid interfaces must be taken into account. Generally, voltage drop is modelled by introducing an effective electrical conductivity [4, 5, 8] in a computational cell adjacent to the metal surface. This approach leads to a mesh-dependent solution.

In this paper, the modified arc root model based on boundary conditions is described. In addition, this paper presents the results of a simple design shape optimization using the developed virtual 3D spark gap model based on local thermal equilibrium assumption and modified arc root model parameters. The simulation results are compared with the experimental data to verify the proposed model.

2 Physical tests for confidence

A high-speed camera is used to obtain arc information through videos with high temporal and spatial resolution. To make this possible, the spark gaps are modified to make the inner processes optically accessible. These preparations are carried out without affecting the functionality of the equipment to ensure comparability. In addition to the high-speed camera, various lenses, optical filters and evaluation software are used to obtain information. This enables examinations of the general arc behaviour, the contour of the arc, and the arc root movement. This experimental method can be used for validation of digital spark gap results.

2.1 Spark gap effects

The high-speed camera captures the events with the voltage and current development over time. Fig. 3 depicts the comparison of two measurements with the same parameters. The current pulse with $I_{8/20} = 500$ A is used for ignition. The prospective short-circuit current has the same value $I_p = 500$ A. The red (dashed) curve shows good behaviour, whereas the blue curve shows a re-ignition event. As a result, there is a drop in the spark gap voltage and a plateau in the arc current.
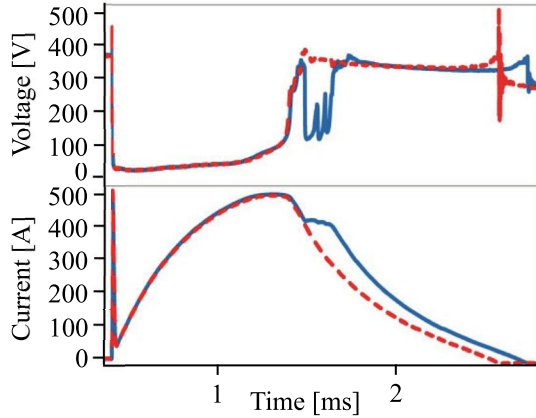

Fig. 3 Comparison of two measurements.

Additionally, this event is recorded with the high-speed camera at the resolution of 336 x 240 px, the framerate of 15 kfps, and the exposure time of 1 μs. By using the camera's trigger signal, the recorded frames can be assigned to the correct position in the timeline, and thus it is possible to observe where the arc is before and after the re-ignition event (Fig.4).
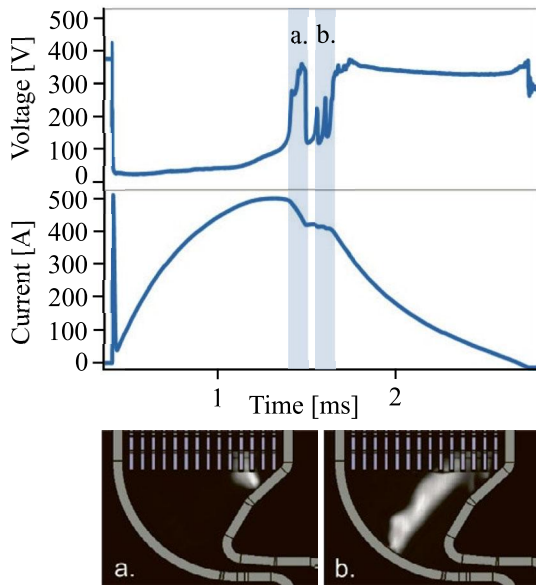

Fig. 4 Visualization of the re-ignition event by frame assignment.

However, such recordings are not able to deliver the physical parameters – e.g. temperature or pressure –

that lead to spark gap effects like this. In the previous example, the re-ignition leads to an increase in specific let-through energy of 13 %. Re-ignition events at current rise can even cause a much higher energy the spark gap has to handle. Hence, understanding spark gap effects is highly relevant for product development as they strongly influence the physical parameters of the device. Digital prototyping offers a possibility to obtain this understanding.

3 Spark gap digital workflow

3.1 Numerical model

CFD code FlowVision is used for the simulating arc ignition, propagation and splitting in the surge protection devices. The software provides automatic mesh generation with local adaptation based on the sub-grid geometry resolution method (SGGR) [9]. The numerical method for calculating the Navier-Stokes equations is based on the finite volume method (FVM) and solves flows with any Mach number in the computational domain [10]. Moreover, this software includes the parallel code architecture with mixed parallelism - simultaneously shared and distributive memory.

3.1.1 Governing equations

The arc phenomenon in gas is characterised by the wide range of physical effects. The most important of these are such as shock waves, ionisation, gas flow with transonic and supersonic velocities, radiation and conjugate heat exchange, the formation of a magnetic field and the generation of pondermotive and Lorentz forces [12]. These physical effects are described by the following system of governing equations.

Mass conservative law (continuity equation):

$$\frac{\partial \rho}{\partial t} + \nabla \cdot (\rho \mathbf{V}) = 0. \tag{1}$$

Moment conservation law (Navier-Stokes equation):

$$\frac{\partial \rho \mathbf{V}}{\partial t} + \nabla \cdot (\rho \mathbf{V} \otimes \mathbf{V}) = -\nabla P + \nabla \cdot \hat{\tau} + \mathbf{F}_L. \tag{2}$$

Energy conservation law:

$$\frac{\partial (\rho H)}{\partial t} + \nabla \cdot (\rho \mathbf{V} H) = \frac{\partial P}{\partial t} + Q_{rad} + Q_{Joule} + \nabla \cdot \left(\frac{\lambda}{C_p} \left(\nabla H - \mathbf{V}(\nabla \cdot \mathbf{V}) \right) \right), \tag{3}$$

here $\hat{\tau} = \mu \left(2\hat{S} - \frac{2}{3}(\nabla \cdot \mathbf{V})\hat{I} \right)$ is the viscous stress tensor, ρ is the density, t is the time, V is the gas velocity, P is the pressure, H is the total enthalpy, μ is the viscosity, $\hat{S}$ is the shear rate tensor, $S_{ij} = \frac{\partial v_i}{\partial x_j} + \frac{\partial v_j}{\partial x_i}$ and $\hat{I}$ – the unit tensor.

The Maxwell steady-state equations for magnetic and electric fields at low magnetic Reynolds numbers and

for electroneutral media has the form shown in the below equations.

Electric charge conservation law (electric current continuity):

$$\nabla \cdot \boldsymbol{j} = 0. \qquad (4)$$

The equation for magnetic induction, induced by electrical current:

$$\nabla \times \boldsymbol{H} = \boldsymbol{j}. \qquad (5)$$

Gauss law (no magnetic charges):

$$\nabla \cdot \boldsymbol{B} = 0. \qquad (6)$$

Electric current density $\boldsymbol{j}$ is specified by Ohm's law and Hall effect

$$\boldsymbol{j} = \sigma(\boldsymbol{E} + \boldsymbol{V} \times (\boldsymbol{B} + \boldsymbol{B}_{ext})), \qquad (7)$$

where $\boldsymbol{E}$ is the electric field strength and σ is the conductivity. Magnetic induction $\boldsymbol{B}$ and magnetic field strength $\boldsymbol{H}$ are linked by the material condition

$$\boldsymbol{B} = \mu_a \boldsymbol{H}, \qquad (8)$$

where μ_a is the absolute magnetic permeability. External magnetic field $\boldsymbol{B}_{ext}$ is an artificial magnetic field that is not simulated but can be set up.

For solving the equations (4-7), the electrical potential ϕ and the magnetic vector potential $\boldsymbol{A}$ are represented as

$$\boldsymbol{E} = -\nabla \phi, \qquad (9)$$

$$\boldsymbol{B} = \nabla \times \boldsymbol{A}. \qquad (10)$$

Substituting (9-10) into (4-7), the equations for the electric potential can be written in the form

$$-\nabla \cdot (\sigma \nabla \phi) + \nabla \cdot \sigma(\boldsymbol{V} \times (\boldsymbol{B} + \boldsymbol{B}_{ext})) = 0 \qquad (11)$$

and for the magnetic potential

$$\nabla \times \left(\frac{1}{\mu_a} \nabla \times \boldsymbol{A}\right) = \boldsymbol{j} \qquad (12)$$

The electric force for the equation (2) is defined by Lorentz and the pondermotive forces

$$\boldsymbol{F}_L = \boldsymbol{j} \times \boldsymbol{B} - \frac{1}{8\pi} \boldsymbol{E}^2 \nabla \varepsilon \qquad (13)$$

here ε is the dielectric permeability of the media. Joule heating in the equation (3) is calculated by

$$Q_{Joule} = \boldsymbol{j} \cdot \boldsymbol{E}. \qquad (14)$$

For the modeling the heat transfer by radiation, so-called P1 model is used

$$\nabla \left(-\frac{4}{3} \frac{1}{\alpha + \beta} \nabla E_r\right) = 4\alpha(\sigma_{rad} \mathrm{T}^4 - E_r), \qquad (15)$$

where σ_{rad} is Stefan-Boltzmann constant, T – the temperature, E_r – the radiation energy density, α and β are the absorption and scattering coefficients for medium. The radiation term in the energy equation (3) equals

$$Q_{rad} = 4\alpha n^2(E_r - \sigma_{rad} \mathrm{T}^4) \qquad (16)$$

and n is the refraction index.

Usually this whole system of governing equations is solved in separate codes [4, 5, 6, 7, 8] - the hydrodynamic subsystem (1-4) and (15) in CFD codes, and the Maxwell equation subsystem (11-12) in other codes. In this work, all systems are solved simultaneously in one code on the same computational mesh. This approach provides more stable solution due to the possibility of using the method of Newton iterations to solve all strongly coupled governing systems.

3.1.2 Modified arc root model

In a thin layer of plasma near the metal (anode or cathode), the condition of plasma electroneutrality is violated. Shielding of the interface with charges leads to a voltage jump at the metal-plasma interface with nonlinear current density-voltage characteristics [5]. Fig.5 shows typical current density-voltage characteristics.
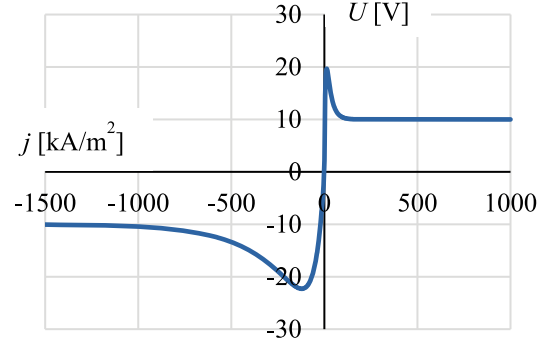
Fig. 5 Current density-voltage characteristics of the electric potential drop between plasma and metal.

As a usual, voltage drop is modelled by introducing an effective electrical conductivity [4, 5, 8] in a cell adjacent to the metal surface. This approach leads to a mesh-dependent solution, the current along the surface could be different than in the real case. In this paper, special boundary conditions are implemented. In this case it is assumed that the layer of voltage drop is very thin and can be neglected. Consider the interface between two substances with the voltage drop U2 and U1 from the left and right sides of the interface (Fig.6).
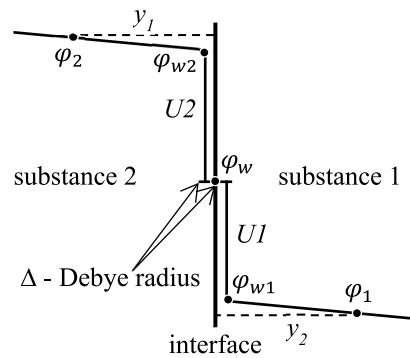
Fig. 6 Schematic diagram of the voltage drop model

Values φ_i, y_i, σ_i in Fig. 6 are the electric potential, the distance from the interface and the conductivity for points i = 1, 2 near both sides of the interface. According to the continuity condition of the normal current density to the interface it leads to

$$j_n = \sigma_1 \frac{\varphi_{w1} - \varphi_1}{y_1} = \sigma_2 \frac{\varphi_2 - \varphi_{w2}}{y_2}, \qquad (17)$$

where $\varphi_{w1} = \varphi_w + U1$ and $\varphi_{w2} = \varphi_w - U2$.

For the equation (11) the boundary values φ_{w1} and φ_{w2} can easily be found, where U1 and U2 are the nonlinear

functions of the current density. The calculation of electric potential is done in two steps. Firstly, the normal current density to the interface is calculated from the previous time step and use for calculating the voltage drop and φ_{w1}. After that, the equation (11) is calculated. For stabilization and accuracy of the simulation, some iterations of these steps can be required.

3.2 Design

Two SPD designs are investigated in this work using digital spark gap prototyping. A goal of the study is to compare functionality of these different designs.
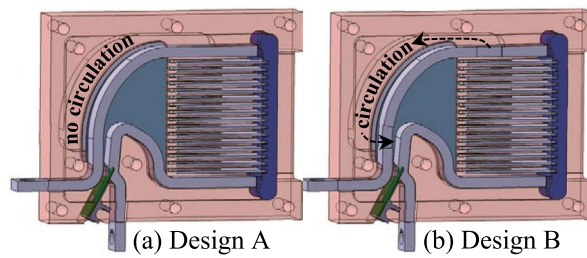

(a) Design A   (b) Design B

Fig. 7 SPD designs: (a) without gas circulation and (b) with gas circulation.
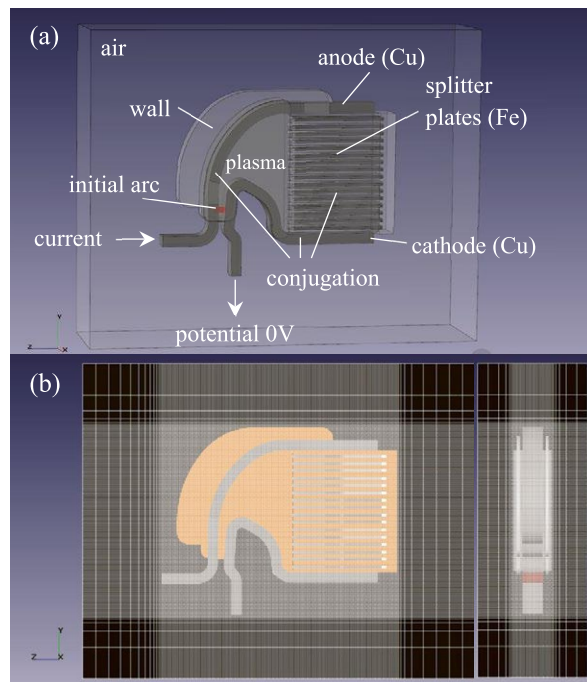

Fig. 8 Simulation model: (a) initial and boundary conditions and (b) computational grid.

As shown in Fig. 7, each geometry consists of two diverging electrodes in the horn and asymmetrical shapes and 16 splitter plates with the V-shaped recess. There is a difference between these two designs. The second geometry includes a channel for gas circulation through the upper electrode, as shown in Fig. 7b.

The upper electrode has openings so that the hot gas from the arc zone flows through the electrode into the special gas channel and back into the arc zone. Compared to the second geometry, the first design (Fig. 7a) has no circulation zone inside and the upper electrode is closed, has no openings. Fig. 8a describes the simulation model, initial and boundary conditions.

The SPD design (Fig. 7b) is imported into the MHD simulation domain, where the thermodynamic and transport properties of the air plasma, the material properties of copper for the electrodes and steel for the splitter plates are considered. These properties are given in the literature [4, 5]. In addition, the splitter plates include non-linear ferromagnetic properties ($\mu_a > 1$) for steel. The geometry takes the position in the centre of a large air box. It is assumed that the magnetic field induced by the electrical arc vanishes on the faces of this box. The additional volume to the magnetic field can be estimated according to the approximation that the magnetic field strength around the current-carrying conductor decreases outwards by $1/r$ [4]. The spark gap simulation includes heat transfer and electromagnetic conjugation between plasma, electrodes, splitter plates and air. At plasma-solid interfaces, the voltage drop is specified as a function of the current density (Fig.5). The cathode roots are treated with the ignition voltage of 22.3 V at the current density of 130 kA/m² and the anode roots have the ignition with 19.6 V at 13 kA/m², whereby the anode is positive and the cathode negative. The modified arc root model is applied here.

Reference temperature of 300 K and reference pressure of 101325 Pa are specified as initial conditions. The ignition of impulse current is not simulated directly in this work. Instead, the arc ignition is carried out by setting the initial temperature 9700 K at the ignition point (Fig. 8a red cylinder) with radius 0.5 mm and thus the corresponding electrical conductivity. The external magnetic field (-0.05, 0, 0) T is applied in the arc run area. The resulting force acts in addition to the Lorentz force and accelerates the arc from the ignition position in the y-direction. This force accelerates the arc of the mains-frequency current in roughly the same way as the impulse current 8/20 μs with 10 kA. The spark gap is applied to the voltage of 230 V with the prospective current of 3.7 kA and ignited with the impulse current at the phase angle of 90 °. These current characteristics are used in the presented spark gap prototyping approach and the input current corresponds to the experimental values according to Fig. 9. The shape of the outlets in the virtual tests are simplified for both designs and the free outlet boundary is used. The presented MHD model is solving on one computational domain. The computational grid is unstructured mesh with about 1.3 mln. cells, where the maximum cell edge size is 6 mm and the minimum size is 0.25 mm.
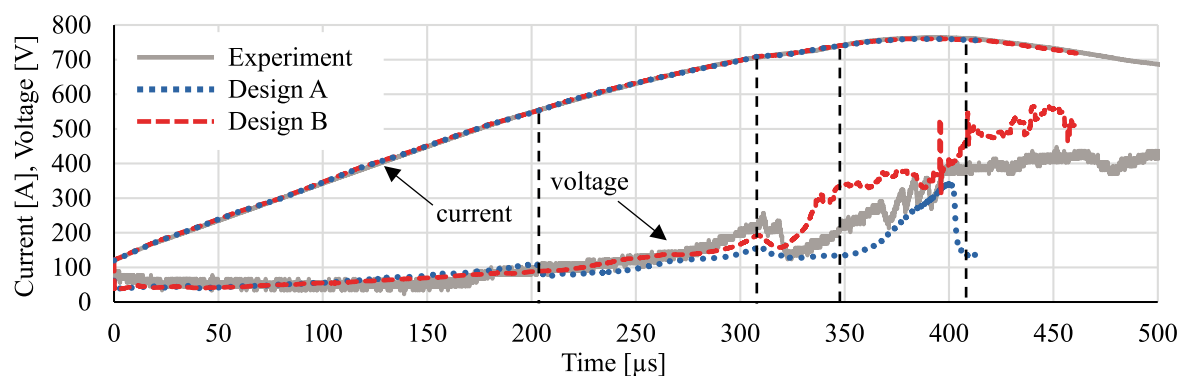
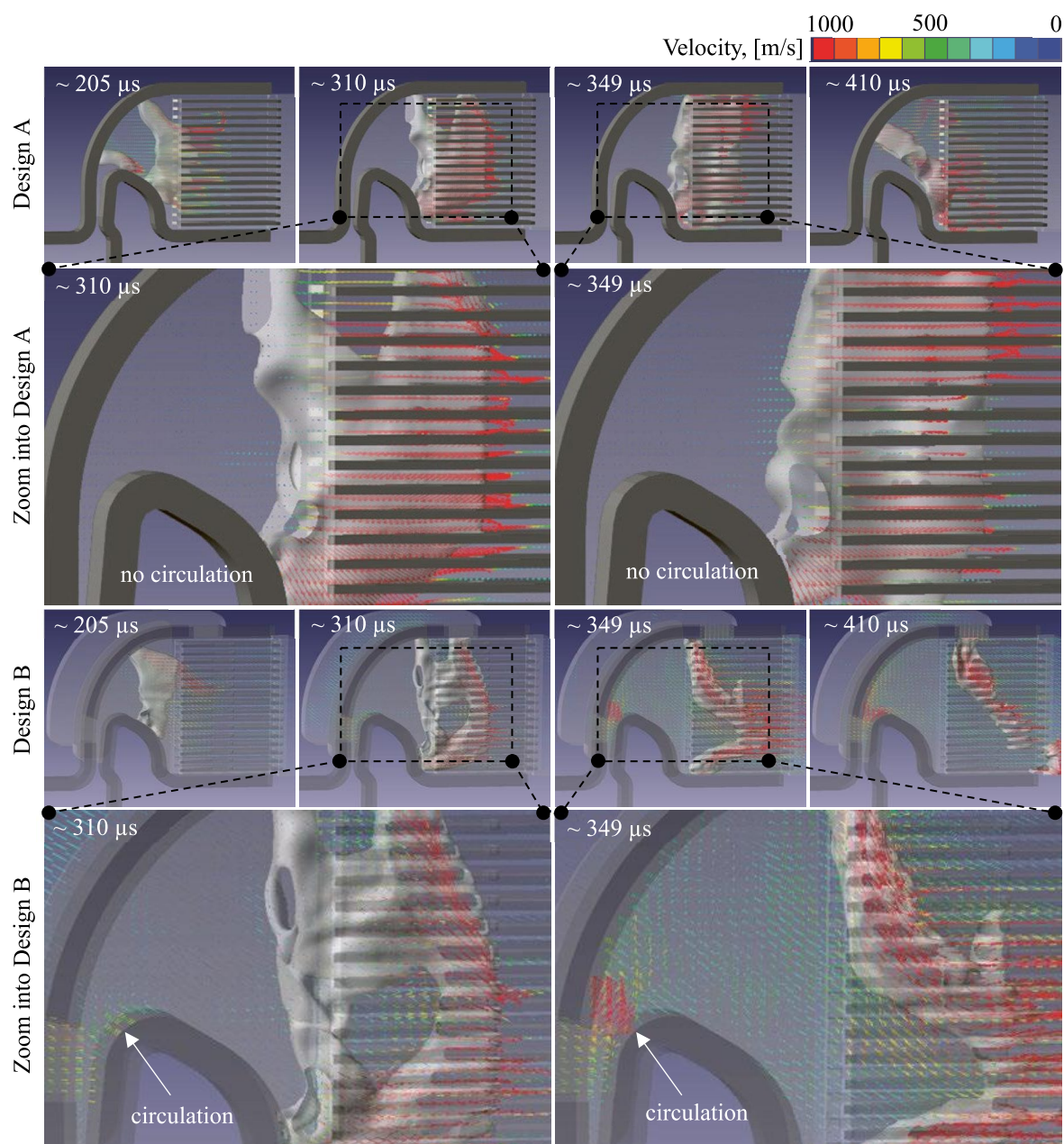**Fig. 9** Comparison of measured and calculated voltage and current.

Fig. 10 Velocity distribution (vectors) visualises gas circulation and current density isosurface (1.5×10^7 A/m^2) shows arc shape in time for Design A and Design B.
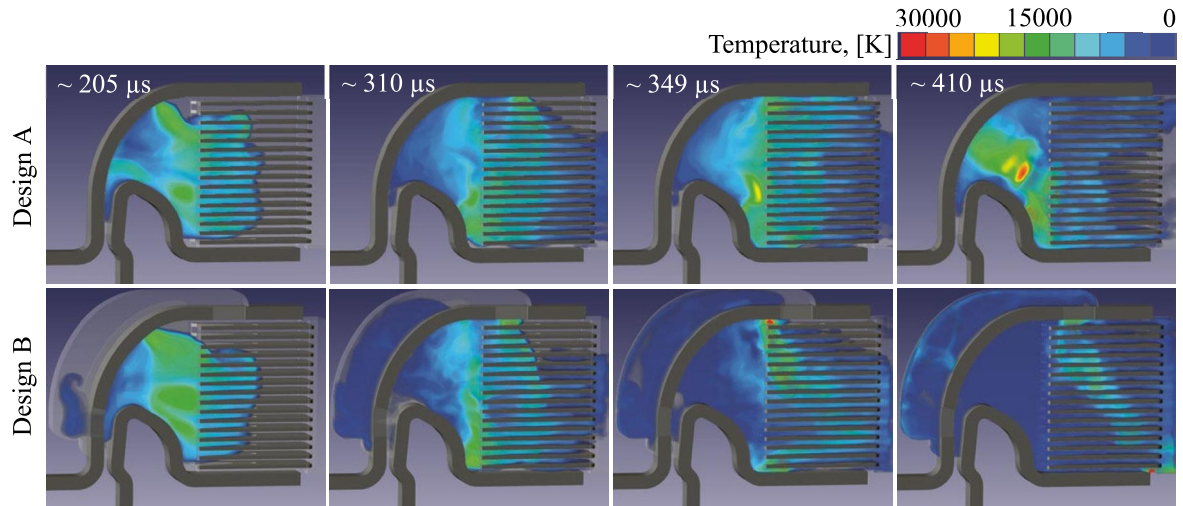
Fig. 11 Temperature distribution in time for Design A and Design B.

4   Results

As shown in Fig. 7, two SPD designs differ in the shape of the upper electrode. Design B has holes in the upper electrode, allowing the gas to circulate inside the SPD product. Design A has no circulation due to the closed electrode shape and the gas cannot flow into the circulation channel.

In Fig. 9, the calculated arc voltages for Design A and Design B are compared to the measurement values. The measurement was carried out on Design B. The arc movement visualization at time steps 205, 310, 349 and 410 μs, as shown in Fig. 10, is used to analyse the voltage profiles for the virtual and physical tests in Fig. 9 in detail. The results for A and B show that the arc movement process towards the splitter plates takes about 310 μs. Between 310-349 μs, the arc for Design B starts to split on the plates and spreads through these plates from about 400 μs. Compared to the experiment (Fig. 9), the results for Design B are in good agreement with the voltage measurement values.

Additionally, the simulation results for Design B show the gas circulation over time (Fig. 10). The velocity visualisation at time 349 μs demonstrates that the gas flows back into the arc area and accelerates the arc splitting process, see Fig. 10 (Zoom into Design B). According to Design A without circulation at time 349 μs, the arc lies close to the plates and does not split at them. In this case, the gas acceleration behind the arc is practically absent, as shown in Fig. 10 (Zoom into Design A).

At time 205 and 410 μs in Fig. 10, the arc in Design A jumps back deep into the arc area and re-ignition effects are observed. The position and shape of the re-ignited arc at 410 μs agree well with the high-speed camera image in Fig. 4b. The re-ignition affects the voltage profiles as it is shown in the experimental curve

in Fig. 4 and in the virtual test for Design A at time 205 and 410 μs shown in Fig 9. The voltage curve drops steeply towards low voltage values. The virtual test for Design A, Fig. 9 also achieves good agreement between experiment and numerical calculation up to 400 μs, but the arc does not split at the splitter plates because of re-ignition, therefore Design A does not satisfy the spark gap requirements.

Fig. 11 shows the temperature distribution over time for Design A and Design B. At time 205 μs, 349 μs and 410 μs, it is clearly seen that the temperature behind the arc in Design B is much lower than in Design A. It is in the range of 300-6000 K, while for Design A the temperature behind the arc at these times is in the range of 6000-17000K. Due to the high temperature in Design A, the re-ignition effect happens very often during the arc movement. Therefore, the gas circulation inside the product helps to lower the temperature and prevent the arc re-ignition.

At time 310 μs, the temperature distribution shown in Fig.11 and the arc shape shown in Fig.10 are almost the same for both designs. In Design B at time 310 μs, shown in Fig. 10 (Zoom into Design B), gas recirculation towards the arc area starts to develop, therefore the gas speed is still very low. The voltage profiles at time 310 μs shown in Fig. 9 demonstrate that the experimental and calculated voltages have almost the same peak shapes. This means that at the 310 μs analysed time the small re-ignition takes place. The re-ignition phenomena are caused due to the high temperature behind the arc and the relatively still cold, almost immobile air between the iron splitter plates.

Comparing the results in time frame 310 μs with time 349 μs, as shown in Fig. 10 (Zoom into Design B), the gas velocity in Design B increases. The gas circulation accelerates and supports the arc splitting process. Furthermore, the circulation cools the gas in the arc area, so that the arc generates less re-ignition and thus less energy in the device.

5   Conclusion

In this paper, two SPD designs were investigated using the developed digital spark gap prototyping model. The following conclusions can be drawn. The virtual spark gap model based on the 3D MHD approach and the modified arc root model has been implemented and validated. The presented MHD model works on one computational domain using FVM. The arc root model is based on boundary conditions, which leads to mesh-independent solution. The investigation of two SPD designs has shown that gas circulation within the spark gap helps to cool the temperature behind the arc, accelerate the arc splitting process and prevent re-ignition. The virtual test with the SPD design including gas circulation agrees well with the experiment, where arc movement and arc splitting are completed. Thus, this design fully satisfies the spark gap requirements. Based on these results, the presented virtual spark gap technology has great potential for further increasing product reliability, performance and size optimisation.

6   Literature

[1] Ehrhardt A., Beier St.: New Deion Chamber for Encapsulated Switchgear, 27th International Conference on Electrical Contacts, June 22 – 26, 2014

[2] Ehrhardt A., Schreiter St., Strangfeld U. and Rock M.: Encapsulated lightning current arrester with spark gap and deion chamber, 19th FSO, Brno, 2011

[3] Chen F., Chang J.: Lecture Notes on Principles of Plasma Processing, Los Angeles: Plenum/Kluwer Publishers, 2002

[4] Rüther J.: Weiterentwicklung und Vereinfachung eines Simulationsmodells für Schaltlicht bögen in Löschblechkammern, Dissertation, TU Braunschweig, 2014

[5] Mutzke A.: Lichtbogen-Simulation unter besonderer Berücksichtigung der Fußpunkte, Dissertation, TU Braunschweig, 2009

[6] Rümpler Ch.: Lichtbogensimulation für Niederspannungsschaltgeräte, TU Ilmenau, 2009

[7] Fuchs R., Mürmann M., Nordborg H.: Towards an efficient arc simulation framework, Plasma Physics and Technology 4(1):79–82, 2017

[8] Benz P, Lichtbogenlauf in einem Leistungsschalter, Presentation, Simulation Conference Schweiz, 2017

[9] Rong M., Yang F., Wu Y., Murphy A. B., Wang W., and Guo J.: Simulation of arc characteristics in miniature circuit breaker, IEEE Trans. Plasma Sci., vol. 38, no. 9, pp. 2306–2311, 2010

[10] Aksenov A, Dyadkin A, Pokhilko V. Overcoming of Barrier between CAD and CFD by Modified Finite Volume Method, Proc. 1998 ASME Pressure Vessels and Piping Division Conference, San Diego, ASME PVP-Vol. 377-2., 1998. pp 79-86

[11] Aksenov A.A., Zhluktov S.V., Savitskiy D.V., Bartenev G.Y., Pokhilko V.I. Simulation of 3D flows past hypersonic vehicles in FlowVision software, Journal of Physics: Conference Series, Volume 653, No. 012072, 2015

[12] Schmidt, George (1979). Physics of High Temperature Plasmas, second edition. Academic Press